PAPER

Nanoscale doping heterogeneity in few-layer WSe$_2$ exfoliated onto noble metals revealed by correlated SPM and TERS imaging

To cite this article: Deep Jariwala *et al* 2018 *2D Mater.* **5** 035003

View the article online for updates and enhancements.

2D Materials

PAPER

Nanoscale doping heterogeneity in few-layer WSe$_2$ exfoliated onto noble metals revealed by correlated SPM and TERS imaging

Deep Jariwala[1,2,3] ⓘ, Andrey Krayev[4], Joeson Wong[1] ⓘ, A Edward Robinson[4], Michelle C Sherrott[1,2], Shuo Wang[5], Gang-Yu Liu[5], Mauricio Terrones[6,7] and Harry A Atwater[1,2]

[1] Department of Applied Physics and Materials Science, California Institute of Technology, Pasadena, CA 91125, United States of America
[2] Resnick Sustainability Institute, California Institute of Technology, Pasadena, CA 91125, United States of America
[3] Department of Electrical and Systems Engineering, University of Pennsylvania, Philadelphia, PA 19104, United States of America
[4] Horiba Scientific, Novato, CA 94949, United States of America
[5] Department of Chemistry, University of California, Davis, CA 95616, United States of America
[6] Department of Physics and Center for 2-Dimensional and Layered Materials, The Pennsylvania State University, University Park, PA 16802, United States of America
[7] Department of Chemistry and Department of Materials Science and Engineering, The Pennsylvania State University, University Park, PA, 16802, United States of America

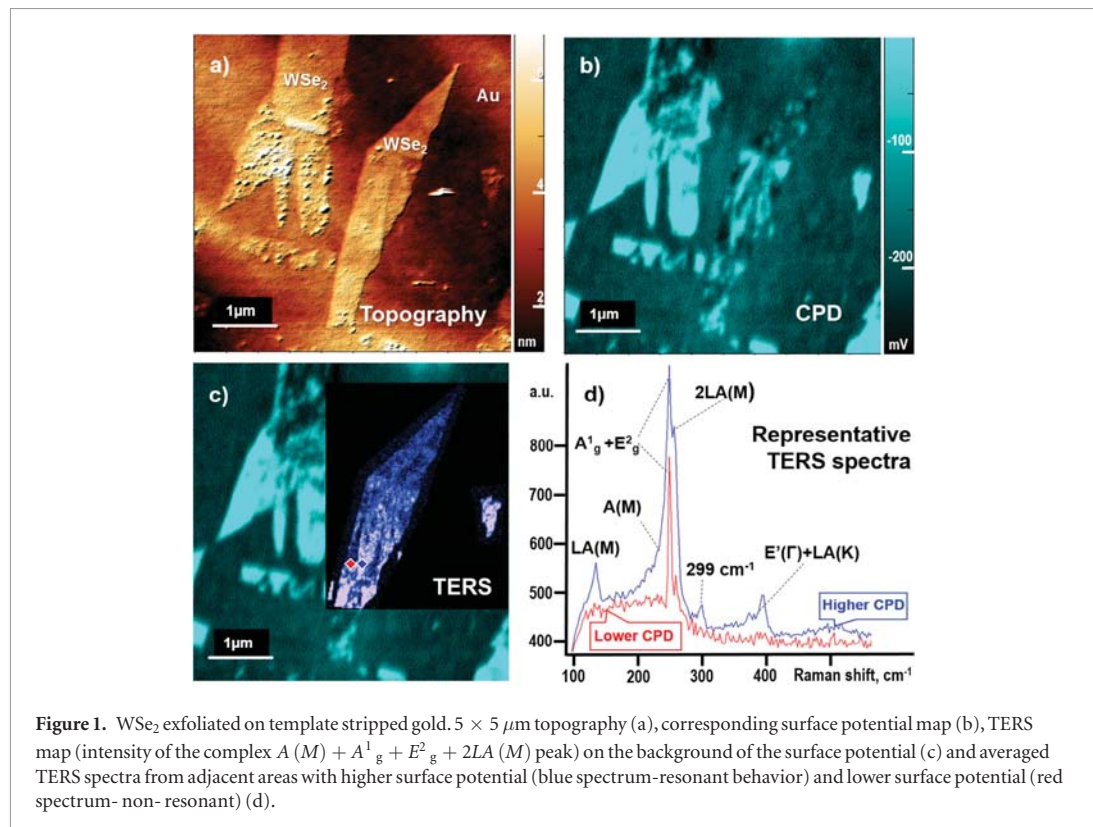**E-mail:** dmj@seas.upenn.edu

Abstract

While extensive research effort has been devoted to the study of the 2D semiconductor–insulator interfaces in transition metal dichalcogenides (TMDCs), there is little knowledge about the electronic quality of the semiconductor–metal interface in the atomically thin limit. Here, we present the first correlated nanoscale mapping of the interface of atomically thin WSe$_2$ with noble metals using co-localized scanning probe microscopy and tip-enhanced optical spectroscopy (TEOS), such as tip-enhanced Raman spectroscopy (TERS). Nanoscale maps of the topography, surface potential, Raman spectra, and the photocurrent amplitude of the WSe$_2$/metal interfaces reveal striking results. Specifically, correlations between surface potential, resonant Raman signatures and photocurrents that indicate the presence of inhomogeneities within interfacial electronic properties, which we attribute to variations in the local doping of the WSe$_2$ likely caused by intrinsic compositional fluctuations or defects. Our results suggest that local electrostatic variations at a lateral scale of 10–100 nm are present even in the highest quality of TMDC crystals and must be considered towards understanding of all interfacial phenomena, particularly in device applications that rely on the buried metal–semiconductor junction interface.

Introduction

The ability to isolate stable, atomically thin layers of materials has stimulated a new field of atomic-scale interface physics, with great potential to create novel interfacial structures of atomically thin materials with novel applications in optoelectronic devices. The transition metal dichalcogenides (TMDCs), are one example of atomically thin materials that has attracted significant attention, owing to their band gaps in the visible part of the electromagnetic spectrum and high luminescence efficiencies in monolayer form. However, integration of TMDCs into optoelectronic devices requires understanding and control of interfaces between metallic and semiconductor layers. While modern commercial semiconductor technologies are based largely on use of bulk semiconductors such as silicon and III–V compound semiconductors, an increasing amount of academic research is dedicated to investigating atomically thin semiconductors for ultrathin devices [1–5].

Since the earliest reports on TMDC-based semiconducting devices, a large body of work has been devoted to the investigation of semiconductor–insulator interfaces, in order to understand charge transport and optimize transistor mobility and current density [6]. Equally important for electronic devices are semiconductor–metal interfaces [7]. The

Figure 1. WSe$_2$ exfoliated on template stripped gold. 5 × 5 μm topography (a), corresponding surface potential map (b), TERS map (intensity of the complex $A\,(M) + A^1{}_g + E^2{}_g + 2LA\,(M)$ peak) on the background of the surface potential (c) and averaged TERS spectra from adjacent areas with higher surface potential (blue spectrum-resonant behavior) and lower surface potential (red spectrum- non- resonant) (d).
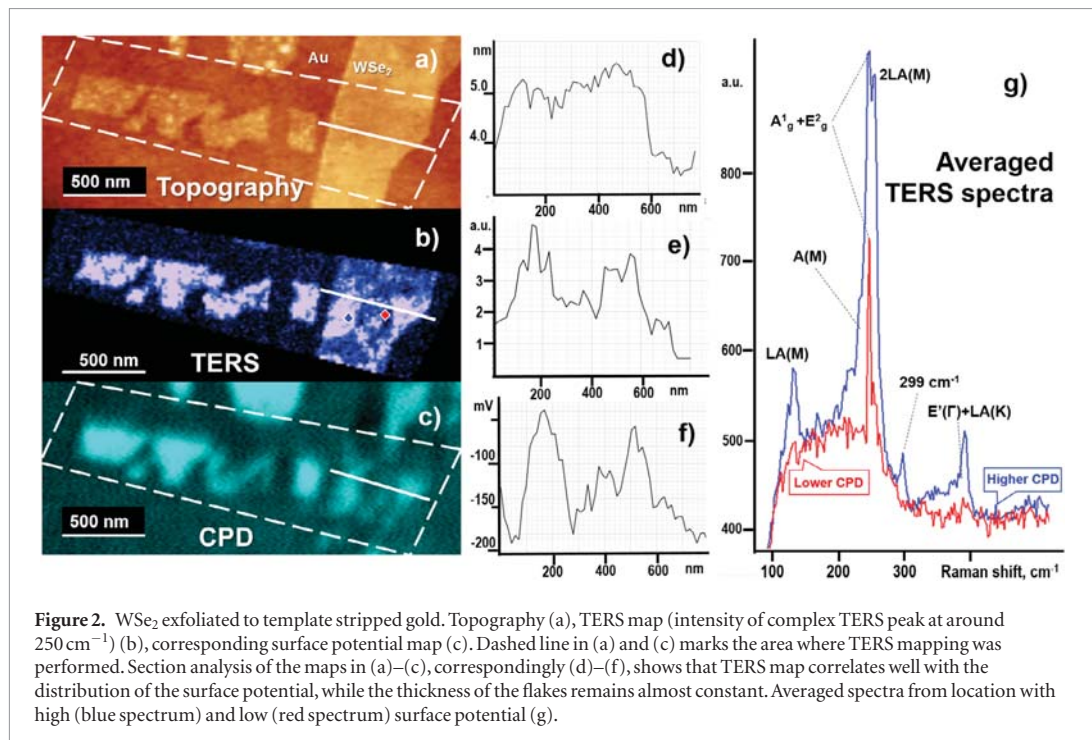
semiconductor–metal interface is the locus of charge carrier injection and collection and is thus critical for improving device performance. While a large body of literature exists about indirect characterization of semiconductor–metal interfaces [7–13], there is much more limited information about directly probing the interface, as sub-surface characterization of buried interfaces in bulk semiconductors is challenging. Two-dimensional (2D) semiconductors, however, provide a new platform for directly probing such interfaces, since the atomically thin nature of the semiconductor prevents complete screening of the electrostatic potentials at a buried interface.

Here, we directly probe interfaces between a 2D semiconductor, WSe$_2$, and noble metals such as gold or silver via scanning probe microscopy and co-localized optical spectroscopy. A key feature of our approach is the cross-correlated spatial mapping of topography, contact potential difference (CPD; which represents the value of local surface potential), photocurrent and tip enhanced Raman scattering (TERS). Briefly, the variation of the resonant frequency of a conductive scanning probe is used to measure variations in surface potential as it scans the surface at a constant tip-sample separation using frequency-modulation Kelvin probe method. Another laser probe is used to excite the tip-sample junction and the scattered light is analyzed for Raman and photoluminescence signals. In addition, the local photocurrent at the tip-sample junction can also be quantified in this technique upon measuring in presence and absence of laser excitation and can be correlated with the Raman and contact

potential measurements. We observe in-plane spatial inhomogeneities of the order of 10–100 nm in the contact potential which correspond to regions of high and low TERS signal. These correlations extend further to positive and negative photocurrents. We attribute the observed inhomogeneities to variations in the local doping, which are both intrinsic to WSe$_2$ and also arise from variations in the contact potential of WSe$_2$ with the polycrystalline metal.

Results and discussion

Samples were prepared by mechanical exfoliation of WSe$_2$ onto either silver or gold substrates of ~120 nm thickness prepared using template-stripping process as detailed in the Material and Methods below [2, 14, 15]. Template stripping regularly and reproducibly gives metal surfaces from evaporated thin films with <1 nm root mean square (rms) roughness values. Low roughness/high smoothness is critical for nanoscale uniformity of contact for an atomically thin, van der Waals 2D material such as WSe$_2$. Roughness in plasmonic metal (e.g. Au, Ag) films can result in localized surface plasmon resonances that can lead to additional absorption or scattering and complicate interpretation of the TERS as well as non-resonant Raman data, hence the choice of template stripped samples. Exfoliation produces a significant number of flakes with thicknesses in the 1–3 nm range, corresponding to 1–4 layers of WSe$_2$ (figure 1). All measurements reported here were performed on the OmegaScope-R coupled to an XploRA confocal

Figure 2. WSe$_2$ exfoliated to template stripped gold. Topography (a), TERS map (intensity of complex TERS peak at around 250 cm^{-1}) (b), corresponding surface potential map (c). Dashed line in (a) and (c) marks the area where TERS mapping was performed. Section analysis of the maps in (a)–(c), correspondingly (d)–(f), shows that TERS map correlates well with the distribution of the surface potential, while the thickness of the flakes remains almost constant. Averaged spectra from location with high (blue spectrum) and low (red spectrum) surface potential (g).
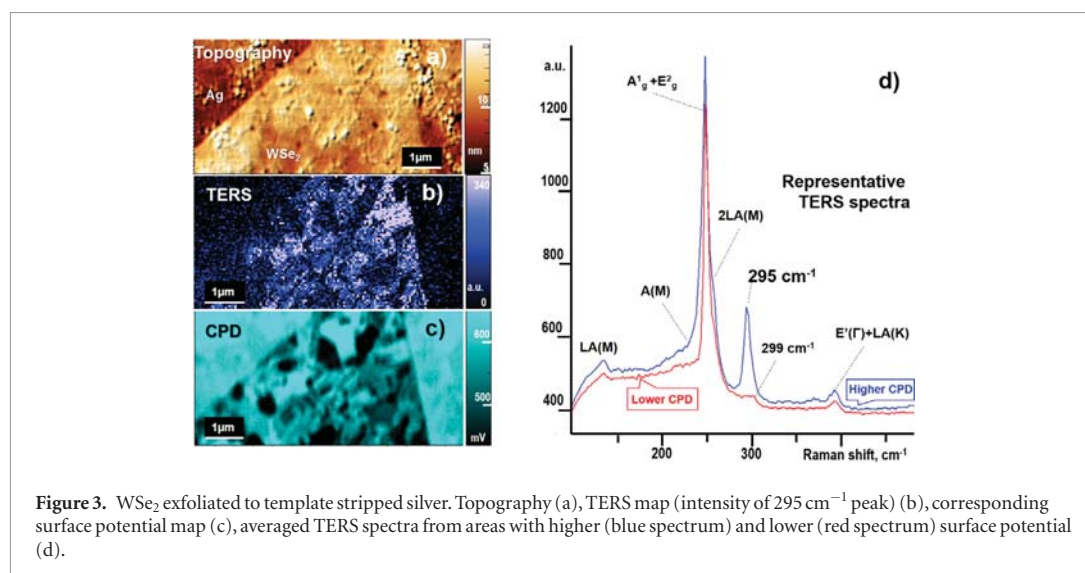
Raman spectrometer (bothHoriba Scientific). Topographic imaging of a representative WSe$_2$ flake on a gold substrate shows a uniform thickness flake of arbitrary shape with sharp edges, suggesting the WSe$_2$ to be single crystalline (figure 1(a)). To map the corresponding contact potential difference, we performed frequency modulated scanning Kelvin probe microscopy (SKM) measurements of the same area of sample. Contact potential difference mapped in this technique represents the distribution of the surface potential across the sample that can arise from intrinsic variations in electronic properties of the material, presence of contamination layers (more typical for metallic surfaces) or both. As shown in figure 1(b), significant inhomogeneities in the contact potential difference were present across the flakes, with the value of variations reaching up to 100 mV between adjacent domains.

To further understand the inhomogeneity in surface potential, a tip enhanced Raman scattering (TERS) map of the same area was acquired with 638 nm excitation laser (1.94 eV), which overlaps with a broad shoulder on the high-energy side of the A exciton [16] in WSe$_2$ and excites resonant Raman response in this material with a number of additional peaks which are not observed with a different excitation wavelength [17] (figure 1(c)). The TERS map showed two distinct types of near-field Raman spectra within the region bounded by the flakes of WSe$_2$, as identified from the topography and CPD maps. The first spectrum, here referred to as the non-resonant spectrum, shows a single Raman band at approximately 250 cm^{-1}, corresponding to the E_{2g} and A_{1g} vibrational modes of WSe$_2$ [17–24]. A second type of spectrum that we observe is

the resonant spectrum. A number of additional Raman modes namely: $LA(M)$ at 135 cm^{-1}, $A(M)$ at 240 cm^{-1}, $2LA(M)$ at 260 cm^{-1} as well as complex peaks at around 375 cm^{-1} and 390 cm^{-1} are observed (figure 1(d)). Observed peaks were assigned specific normal modes based on prior knowledge [17] except for the peak at 135 cm^{-1}, which corresponds to the first-order LA phonon (M point in Brillouin zone), as observed in earlier work [25]. An intriguing observation is that the distribution of intensity associated with complex resonant peaks observed in the 220–280 cm^{-1} range correlates extremely well with the distribution of domains exhibiting higher surface potential, as indicated in the CPD images, whereas the areas with lower surface potential corresponded to non-resonant Raman spectra in the TERS map (figures 1 and 2). We also note that the scale of the heterogeneity of the surface potential and corresponding Raman response makes the latter unobservable by means of conventional confocal Raman microscopy, for which the spatial resolution is limited by diffraction to approximately 400–500 nm at the 638 nm pump wavelength used in our experiments, which is clearly insufficient to resolve domains 10–100 nm in lateral size.

Upon further analysis of the topography with corresponding CPD and TERS maps, it is clear that the differences in Raman spectra and surface potential distribution cannot be explained by thickness variations (number of layers) of the WSe$_2$ flakes. Figure 2(a) shows the topography of a portion of a larger flake that has fairly uniform thickness of approximately 1.5 nm, which, taking into account the thickness of a monolayer to be approximately 0.7 nm, corresponds to bilayer WSe$_2$. Although the thickness is uniform,

Figure 3. WSe$_2$ exfoliated to template stripped silver. Topography (a), TERS map (intensity of 295 cm^{-1} peak) (b), corresponding surface potential map (c), averaged TERS spectra from areas with higher (blue spectrum) and lower (red spectrum) surface potential (d).

the surface potential pattern is non-uniform, with variations between the dark and bright areas as large as 150 mV. The corresponding TERS map (figure 2(b), intensity of complex peak within 220–280 cm^{-1} range) closely resembles the surface potential distribution, showing resonant behavior in regions with higher surface potential and higher intensity of the complex $A(M) + A_{1g} + E_{2g} + 2LA(M)$ peak in areas with higher surface potential. We note that the instrument's spatial resolution of the TERS map is similar to that of the topography image.

In order to determine whether the correlation between the surface potential and resonant-enhanced Raman spectrum is due to the underlying metal or to an intrinsic feature of WSe$_2$ samples, we performed the same measurements on template-stripped silver substrates (figure 3). While we again observed inhomogeneities similar to the WSe$_2$/gold samples, we also observed some interesting differences. The template stripped silver substrate itself has significantly higher inhomogeneity of the surface potential as compared to gold, which may be explained by the large grain size of the silver. We speculate that silver crystals exhibiting different crystallographically oriented planes at the metal/air interface may have oxidized to varying degrees, or may exhibit a strong orientation dependence of the work function. Resonant TERS spectra of WSe$_2$ exfoliated onto silver were also somewhat different from the resonant spectra observed in WSe$_2$ exfoliated onto gold acquired using the 638 nm pump laser as mentioned above. Notably, the relative intensity of the $2LA(M)$ peak decreased for the WSe$_2$ on silver, while an additional peak was observed at about 295 cm^{-1}. To the best of our knowledge, this latter peak has not been reported previously; interestingly, the distribution of the intensity of this 295 cm^{-1} peak correlated the best with the distribution of the surface potential (figure 3). This peak was absent in TERS spectra of WSe$_2$ exfoliated on gold presented in figures 1 and 2, where we observed only weak 299 cm^{-1} peak, which most prob-

ably corresponds to the 302 cm^{-1} band frequently observed in Raman spectra of multilayer WSe$_2$. Further, since the Fermi levels are different in silver and gold, the surface potential of the WSe$_2$ flakes was lower compared to silver, while it was higher compared to gold, implying that on average the flakes are charged differently when exfoliated on gold or silver, but still demonstrated qualitatively similar behavior.
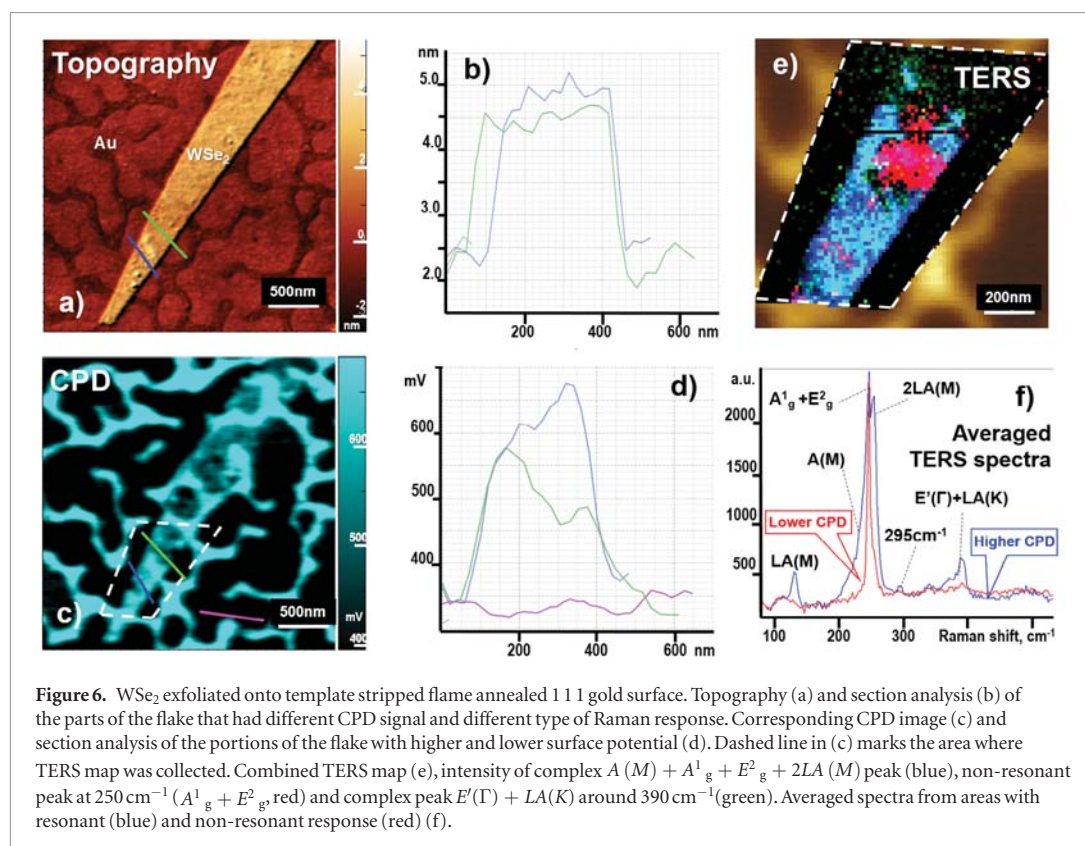
It is well known that depending on the relative orientation of the chalcogenide anions in the upper and lower plane of the individual tri-layers, TMDCs may exist in metastable $1T$ or $1T'$ phases, which are metallic, or in the more stable 2H semiconducting phase [26]. The metallic phases are known to form for a high density of charge donation or electron doping, and are known to show a weaker Raman response compared to the 2H phase [27]. Further, since the resonant Raman response is dominated by excitons that do not exist in the metallic phases, it is possible to have locally formed metallic phase domains that suppress the Raman response in those regions. In order to test this hypothesis, we carried out another set of experiments where the zero-bias photocurrent was recorded concurrently with the TERS and CPD maps. CPD images of the flakes showed the presence of domains with higher and lower surface charge, with corresponding TERS maps again demonstrating resonant behavior in the domains with higher surface potential and non-resonant Raman response in the domains with lower surface potential, both for gold (figure 4) and silver (figure 5) (see supplementary information figures S1 and S2 (stacks.iop.org/TDM/5/035003/mmedia) for TERS maps showing intensity distribution of individual peaks) substrates. Due to a much more uniform distribution of the background surface potential in the gold substrate, SKM images of the WSe$_2$ flakes exfoliated on gold showed more clear contrast compared to the flakes exfoliated on silver. The photocurrent maps recorded simultaneously with the acquisition of the TERS signal clearly show that the non-resonant
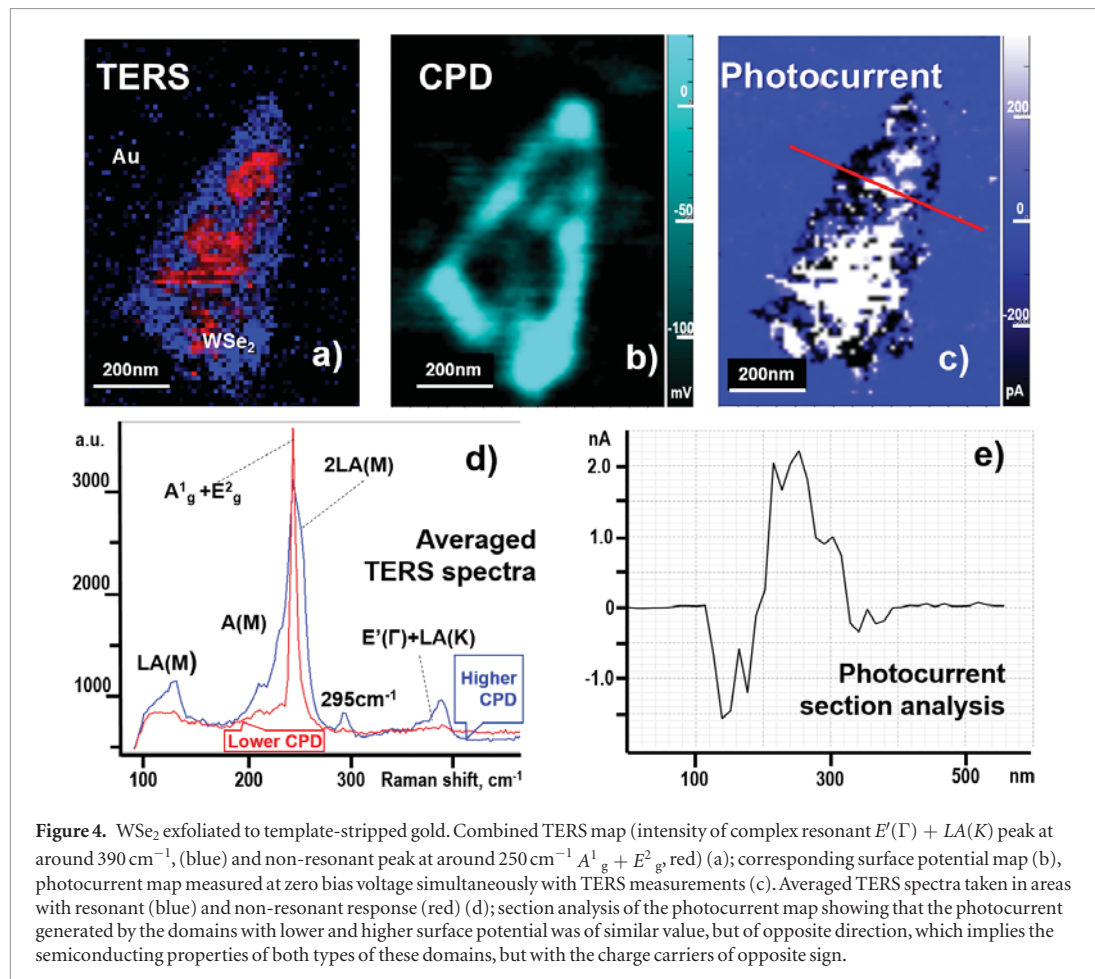
Figure 4. WSe$_2$ exfoliated to template-stripped gold. Combined TERS map (intensity of complex resonant $E'(\Gamma) + LA(K)$ peak at around 390 cm^{-1}, (blue) and non-resonant peak at around 250 cm^{-1} $A^1{}_g + E^2{}_g$, red) (a); corresponding surface potential map (b), photocurrent map measured at zero bias voltage simultaneously with TERS measurements (c). Averaged TERS spectra taken in areas with resonant (blue) and non-resonant response (red) (d); section analysis of the photocurrent map showing that the photocurrent generated by the domains with lower and higher surface potential was of similar value, but of opposite direction, which implies the semiconducting properties of both types of these domains, but with the charge carriers of opposite sign.
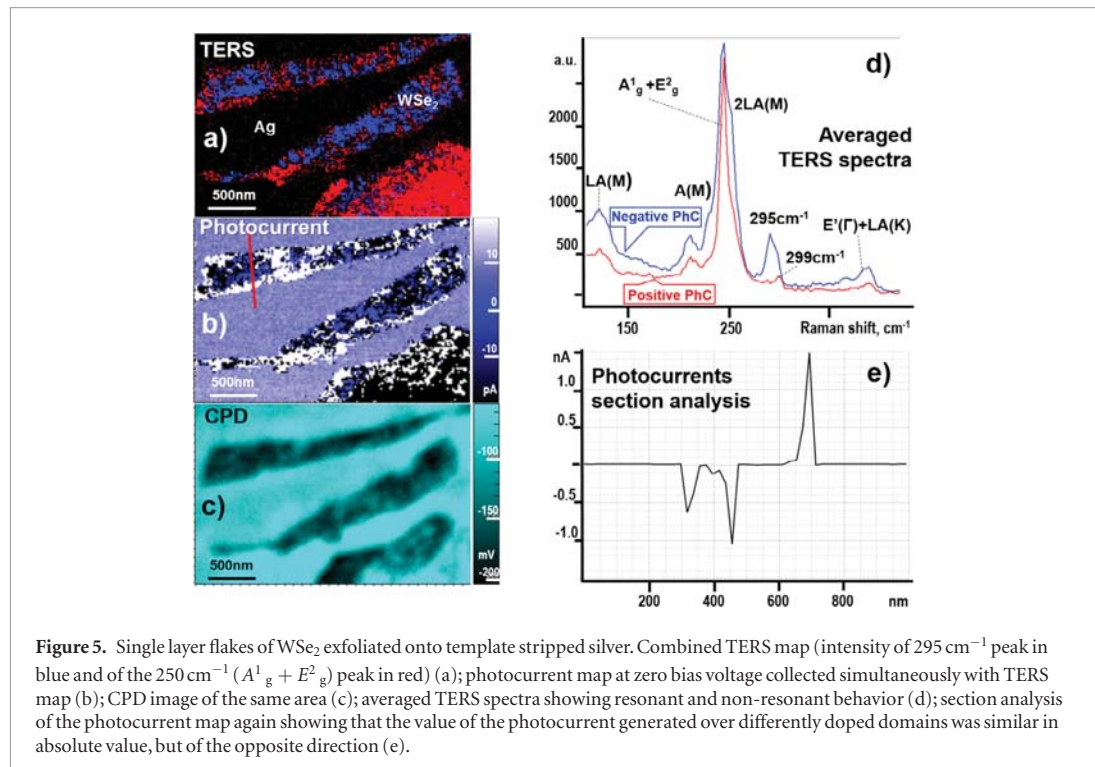
Figure 5. Single layer flakes of WSe$_2$ exfoliated onto template stripped silver. Combined TERS map (intensity of 295 cm^{-1} peak in blue and of the 250 cm^{-1} ($A^1{}_g + E^2{}_g$) peak in red) (a); photocurrent map at zero bias voltage collected simultaneously with TERS map (b); CPD image of the same area (c); averaged TERS spectra showing resonant and non-resonant behavior (d); section analysis of the photocurrent map again showing that the value of the photocurrent generated over differently doped domains was similar in absolute value, but of the opposite direction (e).

Figure 6. WSe$_2$ exfoliated onto template stripped flame annealed 1 1 1 gold surface. Topography (a) and section analysis (b) of the parts of the flake that had different CPD signal and different type of Raman response. Corresponding CPD image (c) and section analysis of the portions of the flake with higher and lower surface potential (d). Dashed line in (c) marks the area where TERS map was collected. Combined TERS map (e), intensity of complex A (M) + A^1 $_g$ + E^2 $_g$ + $2LA$ (M) peak (blue), non-resonant peak at 250 cm^{-1} (A^1 $_g$ + E^2 $_g$, red) and complex peak $E'(\Gamma)$ + $LA(K)$ around 390 cm^{-1}(green). Averaged spectra from areas with resonant (blue) and non-resonant response (red) (f).

domains do not comprise the metallic $1T$ phase, since both types of domains generate a significant amount of photocurrent, though of an opposite sign. This suggests that each type of domain in WSe$_2$ flakes is semiconducting, but each forms a potential barrier of opposite sign relative to the underlying metal. Based on the expected surface charge distribution between coexisting n- and p-doped domains, where electrons from n-doped domains are expected to transfer to p-doped domains to equilibrate the Fermi level, we assign the non-resonant domains with lower surface potential observed in experiments as being p-doped, while the domains demonstrating resonant Raman response and higher surface potential values are assumed to be n-doped. It should be noted that the doping variations in TMDCs may result in significant changes in their photoluminescence response, which implies significant changes in exciton distributions in these materials [28–30]. Since resonant Raman response in TMDC is related to overlapping of the excitation laser or Raman bands with some excitonic band(s), it's not surprising that variations in doping level can result in appearance or disappearance of resonant conditions.

An important question that arises from our results is whether the observed doping heterogeneity is an intrinsic property of exfoliated WSe$_2$ flakes or if it is induced by the substrate, due, e.g. to the polycrystalline nature of gold and silver films used in our experiments or both. We suggest that doping heterogeneity is an intrinsic property in the exfoliated WSe$_2$ flakes, since in the case of the heterogeneity induced directly

by the substrate, the doping should be governed by the local variations of the Fermi level and the sign of the charge passed from the substrate to the flake. But maps of the distribution of the contact potential difference of WSe$_2$ flakes exfoliated onto silver and gold both show similar intra-flake surface potential heterogeneity, despite an overall positive charge of WSe$_2$ on gold relative to the substrate. By contrast, WSe$_2$ flakes exfoliated onto silver are on average charged negatively relative to the substrate (see supplementary information, figure S3), an expected behavior if one accounts for the workfunction in silver ($\sim$4.3 eV) being approximately 0.8 eV lower than in gold ($\sim$5.1 eV) [31].

To further test the possible influence of the polycrystalline nature of substrates on heterogeneities, we performed additional measurements on template stripped, flame annealed gold. Such annealing results in formation of atomically smooth nano-islands with $\langle 1 1 1\rangle$ orientation separated by narrow (few nm) grain boundaries [32]. This experiment was motivated by the following idea: if heterogeneous interface properties on metal surfaces with both random and uniform crystalline orientations are observed, that would demonstrate that these differences are due to intrinsic heterogeneities, rather than being induced by the polycrystalline substrate. Results of this experiment are presented in figure 6. As expected, the substrate was broken into very smooth islands divided by narrow grain boundaries. The surface potential across an individual island was very uniform, while the grain boundaries exhibited significantly increased surface

potential, similar to those observed for MoS_2 flakes suspended over trenches [33]. This increase in surface potential in the WSe_2 flakes over grain boundaries suggests that the underlying substrate and its crystallographic orientation does influence the heterogeneities of the surface potential measured on top of the flake.

We found a narrow tri-layer WSe_2 flake of thickness 2.2 nm (figures 6(a) and (b)) within a single gold nano-island with a surface potential variation and Raman response qualitatively similar to that observed on polycrystalline gold. As was observed for WSe_2 flakes exfoliated onto polycrystalline substrates, the area with lower surface potential resulted in a non-resonant Raman response, while adjacent parts of the same flake located over the same nano-island of gold showed a resonant response (figures 6(e) and (f)) (see supplementary information figure S6 for TERS maps showing intensity distribution of individual peaks). Therefore, we can argue that the polycrystalline nature of the substrate, and the crystalline orientation-specific variation of the surface potential in the metal underlying WSe_2 layers, is not the cause of the observed doping heterogeneity. At the same time we cannot completely exclude the influence of the possible interfacial contaminants (water, organic molecules or local oxidation like in [34]) at the metal/WSe_2 interface on the local doping level in TMDC.

To probe possible influence of interfacial water, we prepared samples in a glovebox under inert, dry atmosphere with water and oxygen levels considerably lower compared to normal ambient conditions (less than 0.5 ppm for both). Despite apparent differences in the preparation conditions, we observed domains with decreased surface potential and non-resonant TERS response in these samples, similar to the samples prepared in ambient conditions (see supplementary information figure S6).

To further probe influence of the exfoliation procedure on the heterogeneity of the transferred flakes of WSe_2, we made samples via heat-assisted transfer, where freshly cleaved thin crystals of WSe_2 attached to a heat-releasing tape were pressed against fresh template-stripped gold surface inside a glovebox, heated to 110 °C for ~1 min to improve the WSe_2-gold adhesion and release the tape. We then briefly (~5 s) sonicated the sample in acetone to remove thick flakes, leaving large areas of mono- to few-layer flakes.

We did observe some variations of the surface potential of flakes obtained via this procedure, though these variations (excluding those corresponding to apparent topographic defects) were considerably smaller (60–80 mV, see supplementary information figure S7) compared to the ones observed in samples prepared via conventional exfoliation performed in the same glovebox from the same bulk crystal (150–200 mV, figure S5). TERS mapping of the heat-assisted samples showed that only the overall intensity of TERS spectra changed across the sample, while the resonant behavior was preserved in the whole TERS map (see supplementary information figure S8).

These observations, (see supplementary information for the summary in form of table S1) suggest that nanoscale doping heterogeneity at TMDC metal interfaces may either be intrinsic to the TMDC crystal or depends on subtle variations in atomic level contact between the TMDC and metal. The accurate origin of the observed heterogeneity, is beyond the scope of the present study and should be a subject of a separate dedicated study.

As a continuation of this work, it would be worthwhile to correlate the optical absorption/scattering or photoluminescence spectra at the nanoscale with local Raman spectra in order to understand why the p-doped domains in WSe_2 do not display a resonant Raman response in conjunction with first principles calculations. Prior literature [35] suggests that selenium-based TMDCs are prone to the formation of Se vacancy sites, or foreign atoms impurities, something that should inevitably affect local doping. In addition, high resolution structure characterization using electron microscopy would complement understanding of dopants and defects at the atomic scale. In addition, first principles calculations combined with electrostatic charge transfer/band diagram calculations should also help understand the exact nature of the heterogeneity.

Conclusions

We report that interfaces between mono-to-few-layer flakes of WSe_2 and template-stripped silver or gold are non-uniform at the nanoscale. Analysis of the experimental data suggests that the observed non-uniformities arise from crystalline intrinsic variations in the WSe_2 material properties over a scale of 50–200 nm rather than from the surface potential variation caused by different crystalline facets of underlying gold or silver. However, the influence of the interfacial contaminants cannot be excluded at this time. Correlated SKM, TERS and photocurrent mapping of the flakes revealed domains ranging in size from a few tens-to a few hundreds of nanometers, much below the diffracted limited resolution obtained in far-field confocal microcopy. The observed are interpreted as having complementary doping type, as each type of domain demonstrated significant photocurrent of similar absolute magnitude, but of opposite sign. The TERS spectra of n-doped domains demonstrated resonant behavior typical for excitation with a 638 nm laser, while the TERS spectra of p-doped domains were mostly dominated by a single peak at approximately 250 cm^{-1}, which is typical for the non-resonant Raman response of WSe_2. In summary, our results emphasize the importance of nanoscale characterization of uniformity of the optoelectronic properties of TMDC layers, specifically when they are intended to serve as an active material for photovoltaic and other device applications.

Materials and methods

Materials

All materials were used as received unless specifically described. H_2 at 99.99% purity was purchased from Praxair, Inc. For preparation of Au thin films, Au slugs (99.99%, Alpha Aesar Premion Co.) and mica (highest grade, Ted Pella) were used. Epoxy glue (Epo-tek 377) was purchased from Epoxy Technology. Ultrapure water ($\geqslant$18 MΩ, Millipore Milli-Q) and 200 proof ethanol (Gold Shield Chemical Co.) were used for washing Si wafer. WSe_2 single-crystals (99.995%, lightly p-doped) were commercially purchased from HQ graphene and exfoliated using Scotch tape both inside and outside a nitrogen glove box.

Preparation of ultraflat gold thin films

A thin layer of mica was peeled from each mica sheet to explore a fresh mica (0 0 0 1) surface. Those mica sheets were immediately placed into a high-vacuum evaporator (Denton Vacuum, model 502-A) [36]. These mica sheets were heated to 350 °C under a base pressure of 2.2×10^{-6} Torr. The Au was thermally vaporized and deposited onto mica surfaces at 0.3 nm s^{-1}. The thickness of Au films used for this investigation was 100 nm. After evaporation, the Au was annealed *in situ* at 365 °C for 30 min to increase the size of the Au (1 1 1) terraces [37]. After annealing, the Au/mica samples were allowed to cool overnight at a pressure of 2.2×10^{-6} Torr.

The preparation of template stripped gold thin film on Si wafer surfaces follows a method reported previously. Briefly, the gold films were treated using H_2 flame in order to remove impurities on Au surfaces, and to improve terrace size [38]. A small droplet of epoxy glue was placed to each of the Si wafer surfaces (pre-cleaned and dried). The Au side of the Au/mica sheet was pressed to glue covered Si surfaces and allowed to cure at 150 °C for 1 h. The Au surfaces were generated by peeling mica off, and the Au (1 1 1) surfaces facing mica previously exhibit ultraflat morphology in comparison to Au thin films prepared by other means [39]. The subsequent treatment and measurements using these Au surfaces are described in a later section. The same template stripping procedure was adopted for other samples but the Au was evaporated also on a Si wafer (precleaned and dried). In this case the template stripped Au surface had a polycrystalline texture unlike the ones grown on Mica

Scanning probe microscopy and spectroscopy

Scanning probe microscopy and TERS characterization was performed on OmegaScope-R SPM (AIST-NT, now-Horiba Scientific) coupled to XPlora confocal Raman microscope (Horiba Scientific). HQ NSC-14-Cr/Au probes (Mikromasch) were used for SKM characterization, OMNI-TERS-FM probes (APP

Nano) were employed for TERS imaging. All Raman measurements were performed with 638 nm laser, the power on the sample was within the 60–100 μW range. The wavelength of the feedback laser in AFM registration system was 1310 nm.

Kelvin probe imaging was performed in frequency modulation mode which allowed improved spatial resolution of the distribution of the contact potential difference (which reflects the distribution of the surface potential on the sample). The value of the surface potential of the probes was not calibrated, so it was the contrast in the CPD images, not the absolute value of the surface potential, which bore the physical meaning in the CPD images.

Photocurrent that was recorded simultaneously with TERS data was measured across the WSe_2 flakes at zero bias, when the substrate and the conductive TERS probe served as the electrodes. 10 MΩ resistor was connected in series with the electrode clamp that went to the gold/silver substrate surface in order to prevent excessive current that can be potentially damaging for the TERS tips. Both the negligible current response over bare gold/silver areas and significant current observed over WSe_2 flakes, confirmed that the TMDC material acted as an active photovoltaic device, while the tip and the substrate just served as passive electrodes.

ORCID iDs

Deep Jariwala ⓘ https://orcid.org/0000-0002-3570-8768
Joeson Wong ⓘ https://orcid.org/0000-0002-6304-7602

References

[1] Jariwala D, Sangwan V K, Lauhon L J, Marks T J and Hersam M C 2014 *ACS Nano* **8** 1102–20
[2] Jariwala D, Marks T J and Hersam M C 2017 *Nat. Mater.* **16** 170–81
[3] Bhimanapati G R *et al* 2015 *ACS Nano* **9** 11509–39
[4] Grigorieva I V and Geim A K 2013 *Nature* **499** 419–25
[5] Fiori G *et al* 2014 *Nat. Nanotechnol.* **9** 768–79
[6] Li S-L, Tsukagoshi K, Orgiu E and Samorì P 2016 *Chem. Soc. Rev.* **45** 118–51
[7] Allain A, Kang J, Banerjee K and Kis A 2015 *Nat. Mater.* **14** 1195–205

[8] Liu W, Kang J, Sarkar D, Khatami Y, Jena D and Banerjee K 2013 *Nano Lett.* **13** 1983–90

[9] Kang J, Liu W, Sarkar D, Jena D and Banerjee K 2014 *Phys. Rev. X* **4** 031005

[10] Das S, Chen H-Y, Penumatcha A V and Appenzeller J 2012 *Nano Lett.* **13** 100–5

[11] Chen J-R *et al* 2013 *Nano Lett.* **13** 3106–10

[12] Kappera R *et al* 2014 *Nat. Mater.* **13** 1128–34

[13] Wu C-C, Jariwala D, Sangwan V K, Marks T J, Hersam M C and Lauhon L J 2013 *J. Phys. Chem. Lett.* **4** 2508–13

[14] Jariwala D, Davoyan A R, Tagliabue G, Sherrott M C, Wong J and Atwater H A 2016 *Nano Lett.* **16** 5482–7

[15] Wong J *et al* 2017 *ACS Nano* **11** 7230–40

[16] Arora A *et al* 2015 *Nanoscale* **7** 10421–9

[17] del Corro E *et al* 2014 *ACS Nano* **8** 9629–35

[18] Zhao W *et al* 2013 *Nanoscale* **5** 9677–83

[19] Late D J, Shirodkar S N, Waghmare U V, Dravid V P and Rao C N R 2014 *Chem. Phys. Chem.* **15** 1592–8

[20] Thripuranthaka M, Kashid R V, Sekhar Rout C and Late D J 2014 *Appl. Phys. Lett.* **104** 081911

[21] Sanghun K, Kangwon K, Jae-Ung L and Hyeonsik C 2017 *2D Mater.* **4** 045002

[22] Saito R, Tatsumi Y, Huang S, Ling X and Dresselhaus M S 2016 *J. Phys.: Condens. Matter* **28** 353002

[23] Qing-Hai T *et al* 2017 *2D Mater.* **4** 031007

[24] Chakraborty B, Matte H S S R, Sood A K and Rao C N R 2013 *J. Raman Spec.* **44** 92–6

[25] Park K-D, Khatib O, Kravtsov V, Clark G, Xu X and Raschke M B 2016 *Nano Lett.* **16** 2621–7

[26] Ambrosi A, Sofer Z and Pumera M 2015 *Chem. Commun.* **51** 8450–3

[27] Ma Y *et al* 2015 *ACS Nano* **9** 7383–91

[28] Li C H, McCreary K M and Jonker B T 2016 *ACS Omega* **1** 1075–80

[29] Ross J S *et al* 2013 *Nat. Commun.* **4** 1474

[30] Neupane G P *et al* 2017 *ACS Appl. Mater. Interfaces* **9** 11950–8

[31] Michaelson H B 1977 The work function of the elements and its periodicity *J. Appl. Phys.* **48** 4729–33

[32] Yang G, Qian Y, Engtrakul C, Sita L R and Liu G-Y 2000 *J. Phys. Chem. B* **104** 9059–62

[33] Robinson B J, Giusca C E, Gonzalez Y T, Kay N D, Kazakova O and Kolosov O V 2015 *2D Mater.* **2** 015005

[34] Smithe K E *et al* 2018 *ACS Appl. Nano Mater.* **1** 572–9

[35] Addou R and Wallace R M 2016 *ACS Appl. Mater. Intfaces* **8** 26400–6

[36] Riposan A, Li Y, Tan Y H, Galli G and Liu G Y 2007 *J. Phys. Chem. A* **111** 12727–39

[37] Qian Y L, Yang G H, Yu J J, Jung T A and Liu G Y 2003 *Langmuir* **19** 6056–65

[38] Wadu-Mesthrige K, Amro N A and Liu G Y 2000 *Scanning* **22** 380–8

[39] Hegner M, Wagner P and Semenza G 1993 *Surf. Sci.* **291** 39–46